The effect of reinforcement particle size on the mechanical and fracture properties of glass matrix composites

Yangyang Cai, Zheng Liu, Keqian Gong, Yong Zhang [*]

Beijing Key Laboratory of Fine Ceramics, State Key Laboratory of New Ceramics and Fine Processing, Institute of Nuclear and New energy Technology, Tsinghua University, Beijing, 100084, China

A B S T R A C T

The strength and toughness of sealing glass are currently unable to meet increasingly severe application conditions, and composites are an effective way to solve this problem. The size of reinforcement particles significantly affects the material properties, while the underlying mechanism still eludes deeper understanding. In this paper, the influence of the embedded alumina size is investigated from the perspectives of mechanical and fracture properties by mechanical tests, fracture toughness tests and the finite element method. The results of the experiment and simulation indicate that the fracture energy is mainly consumed by interface debonding and particle breakage, and the former consumes more energy. Materials with large particles have better mechanical properties, while those with small particles have better fracture properties. This difference could be ascribed to the curvature of the particles rather than the size. Therefore, an ideal reinforcement particle shape with both mechanical and fracture advantages is proposed. The results shed light on the nature of particle enhancement and point out a new direction for the design of sealing glass composites.

1. Introduction

Sealing glass is an advanced insulating material that has a combination of improved mechanical and chemical properties, such as higher temperature resistance, better corrosion resistance, radiation resistance and aging resistance [1]. It has been applied in the fields of fuel cells, metal/ceramic connections, feed-through seals, hermetic connectors, and transducers [2–4]. Sealing glass is the most critical material in components such as electrical penetration assemblies (EPAs) of high-temperature gas-cooled reactors, so increasing its strength can improve the service stability and life of the components. Composite materials show outstanding strengthening effects and have been successfully applied to the modification of aluminum [5–9], polymers [10–13] and glass [14–16]. Understanding the influence of the damage evolution in composite materials on structural properties is helpful to maximize their potential.

Reinforcement materials affect the properties of composites through the reinforcement characteristics, bonding interfaces with the matrix, size, shape, etc. The characteristics of the reinforcement can be reflected in the composites, for example, the addition of metal particles can enhance toughness [17]. Different reinforcement shapes affect the stress distribution in the material, thus affecting the performance [18], and the volume fraction of the reinforcement usually has an optimal value [19]. In glass, materials such as SiC [14, 20], Al_2O_3 [16,21], Si_3N_4 [22] and thoria [23] are often used as reinforcement particles. Al_2O_3 can be well wetted by glass and form a

---

strong bond [14], and alumina can be used as a carrier of Cr ions for photoluminescence spectroscopy techniques to measure the stress in the glass to realize the integration of structure and function [24]. It is well known that stress concentration in glass can lead to devastating consequences, so local excessive stress should not be introduced during enhancement. Composites inevitably undergo heat treatment during the manufacturing process, and the coefficient of thermal expansion (CTE) is a key factor affecting the stress in composites. Tensile stress can easily lead to glass damage, if the CTE of the matrix (α_m) is less than that of the reinforcement (α_r), an unbearable tensile stress is generated near the glass during the cooling process. If α_m is greater than α_r, compressive stress is generated in the glass near the particles during the cooling process. However, the stress distribution leads to cracks along the radial direction of the particles, and the cracks can easily connect, resulting in the overall failure of the material. Therefore, α_r should be carefully selected to attain a balance between enhancement and deterioration. The CTE of alumina is similar to that of glass, and considering its strength and bonding performance, Al_2O_3 was selected as the reinforcement particle in this study. The shape of the reinforcement particles affects the properties of composites, and positions with acute angles are prone to stress concentration and crack initiation [25]. Therefore, smooth spherical particles are an ideal choice.

It is widely accepted that the size of reinforcement particles affects the properties of composites, especially the alumina-glass system, but the internal mechanism is still controversial [16,26]. Due to residual thermal stress, there is a maximum critical diameter of reinforcement particles, exceeding which will lead to a rapid deterioration of performance [27]. However, some people suggest that below the critical size, reinforcement particles, similar to bubbles, are 'inherent flaws' in glass, so large particles are more harmful [23,28]. Furthermore, smaller reinforcements elevate the densification level and microstructural uniformity, thereby improving the hardness and wear resistance [29]. In addition, small particles improve the performance of composites by reducing defects around the particles [30] and increasing the specific surface area to enhance load transfer [11]. Lloyd even believes that the fracture strength is inversely proportional to the square root of the particle size [31]. On the other hand, reinforcement particles can also be seen as 'pinning positions', so the larger they are, the more effective they are in pinning the crack front [21]. Diler et al., using a central composite design approach, concluded that large reinforcement particles should be preferentially used to obtain high wear resistance [32]. Wang et al. found that the hardness and fracture toughness of large reinforcement particles (6–12 μm) were significantly higher than those of small particles (2–3 μm) due to crack deflection and bridging [33]. In addition, some studies only found an optimal particle size [34,35]. The above contradictions are mainly because the influence mechanism of particle size on the properties of composites has not been unified.

Here, the effect of reinforcement particle size on the properties of composites was investigated in terms of mechanical and fracture properties by means of a combination of experiment and simulation. The reasons for the contradictions in previous studies are explained, and new solutions are proposed to provide new insights for manufacturing glass matrix composites with better performance.
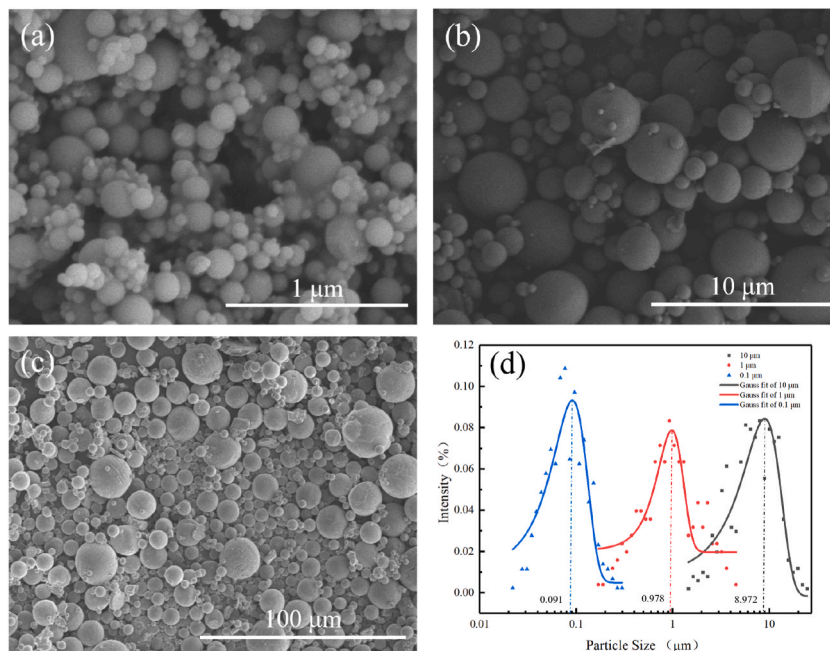
Fig. 1. (a–c) Morphology of Al_2O_3 powders with an average particle size of 0.1, 1 and 10 μm, respectively. (d) Particle size distribution.

2. Experimental procedure

2.1. Sample preparation

The sealing glass used is TH-3 from State Key Laboratory of New Ceramics and Fine Processing, China, which is a commercial borosilicate glass. The TH-3 was prepared by the melt-quenching method. The raw materials are fully mixed in a planetary ball mill and then melted in a platinum crucible at 1500 °C for 5 h. The molten glass was quickly poured into cold deionized water to form glass frits. Subsequently, the glass frits were dried and ball milled with ethanol in a grinding container. The obtained powder was mixed with an appropriate amount of organic binder to form granulated glass powders, and detailed preparation process was reported previously [36, 37]. The sintered glass without reinforcement was labeled GC1. Then, these granulated glass powders were mixed with α-Al$_2$O$_3$ powder (RUISiL, China) to obtain composite samples containing reinforcements with an average particle size of 0.1, 1, and 10 μm, then sintered and denoted GC2, GC3 and GC4, respectively. The particle size distribution of Al$_2$O$_3$ is shown in Fig. 1. Taking into account the effect of amplifying the reinforcement and avoiding its aggregation, the addition level of 20 wt% was selected. The powders with reinforcements were fully ground in an agate mortar for 20 min, compacted and broken 3 times to thoroughly mix the reinforcements and the matrix, and then put into molds for compaction. The samples were sintered in a muffle furnace (SX2-5-12, CHOY, Shanghai, China) to remove the binder. The binder discharge process was as follows: heating to 400 °C at a rate of 2 °C/min, then heating to 700 °C at a rate of 2.5 °C/min, and maintaining for 1 h, then cooling in the furnace at an air atmosphere. Then, sintering at higher temperature was carried out to obtain composites. The process was as follows: heating to 880 °C, 920 °C, 960 °C, and 1000 °C at a rate of 10 °C/min, respectively, and retaining for 0.5 h at the selected temperature, then cooling to 560 °C at a rate of 15 °C/min with 1 h soaking time, then cooling down in the furnace. The process was carried out in a horizontal furnace in a nitrogen atmosphere with a flow rate of 1000 ml/min. The temperature maintenance stage at 560 °C was implemented for the elimination of residual stress in the glass matrix composites.

2.2. Testing methods

2.2.1. Hardness and fracture toughness

The samples were sintered into a cylinder with a diameter of 5 mm and a height of 5 mm in a graphite mold. One of the surfaces was successively ground with silicon carbide abrasive papers of 100, 180, 320, 600, 1000, 2000, and 3000 grit, polished with zirconia polishing solution, and then ultrasonically cleaned for 5 min. Samples GC1, GC2, GC3 and GC4 were tested for hardness with a Vickers hardness tester (FM-810, FUTURE-TECH, Japan) under the load of 1.0 kgf; 20 points were tested for each sample, and the average values and standard deviations were calculated. The fracture toughness of the samples was determined by the indentation method. The samples were indented with a Vickers indenter on an indentation instrument (HV-502, Shanghai Daheng Optics and Fine Mechanics Co., Ltd., China) under a load of 10 N with a dwell time of 10 s at room temperature, producing clear radial cracks on the samples. The microstructure of the cracks was observed by field emission scanning electron microscopy (FE-SEM) (SU8220, Hitachi, Japan), and the crack length was measured by ImageJ software. Fracture toughness (K$_{IC}$) was calculated using the model of Anstis et al. [38] according to the following equation:

$$K_{IC} = 0.016(E/H)^{1/2}PC^{-3/2} \tag{1}$$

where E is the elastic modulus, H is the hardness, P is the load, and C is the half length of the indentation crack. A total of 120 crack lengths were measured, and the average values and standard deviations were obtained.

2.2.2. Compression test and shear test

The samples used for the compression test were sintered with a graphite mold to obtain a cylinder with a diameter of 5 mm and a height of approximately 5 mm. The sintered samples were reduced in thickness to 4 mm by grinding both sides to eliminate possible contamination by the graphite die. A universal testing machine (WDW-100, SHIMADZU, Jinan, China) was used to carry out the compression test at a rate of 0.05 mm/min to obtain the stress peak and load–displacement curve. The glass samples in the shear test were sintered with an Al$_2$O$_3$ plate using a graphite mold. The size of the Al$_2$O$_3$ plate was 5 × 10 × 30 mm, and the glass was a cylinder with a diameter of 5 mm and a height of 5 mm. The shear strength of the interface between the Al$_2$O$_3$ and the glass was measured using a mold to peel the glass from the tangential direction [39]. Each batch included 20 samples to obtain the average strength and standard

Table 1
Parameters in the DMA test.

Content	Parameters
Module	Multi-frequency-strain
Clamp	3-point bending
Span (mm)	20
Atmosphere	Air
Frequency (Hz)	1
Heating rate (°C/min)	5
Temperature range (°C)	25~400

deviation, and abnormal data were removed [40,41].

2.2.3. Dynamic mechanical analysis

Dynamic mechanical analysis (DMA) (Q800, Waters, America) was used to measure the dynamic mechanical properties of the materials at different temperatures. The samples were sintered into a cuboid and processed to a strip of $3 \times 10 \times 30$ mm on a grinder. The test parameters are shown in Table 1.

2.3. Microstructure characterization

The microstructures of the samples and fracture surfaces were characterized by FE-SEM (SU8220, HITACHI, Japan). The particle size and porosity were obtained by ImageJ software.

2.4. Finite element analysis

Square two-dimensional microstructure models were developed using the commercial finite element analysis software ABAQUS, and cracks were preset to simulate crack propagation using the extended finite element method (XFEM). XFEM is an extension of the conventional finite element method, with the difference that it allows the presence of discontinuities in an element by enriching the degrees of freedom with special displacement functions [42]. The boundary conditions and loads are shown in Fig. 2, and the red and blue triangles represent fixed and free boundaries, respectively. To simulate the interface debonding process, three material models of the matrix (glass), reinforcement particles (Al_2O_3) and interface were established and assigned to the corresponding position. The interface thickness was taken as 1/10 of the particle diameter according to the microstructure. The three materials were considered brittle, and therefore, the maximum principal stress damage form of the traction separation law was adopted. The mechanical and physical properties used in this model are shown in Table 2. The Young's modulus was measured by a nanoindentation instrument (Keysight Technologies, G200, China) with an XP-TB26649-2106 tip and an indentation depth of 900 nm. The data are the average of three points. The changes in the CTE of the glass with temperature were measured by a Netzsch Instrument (Netzsch Instruments North America, LLC, Burlington, MA) 402 dilatometer over a temperature range of 20–500 °C at a heating rate of 5 °C/min in an argon atmosphere at a flow rate of 60 ml/min, which can be found in publicly available data. The maximum principal stress of the interface was obtained by shear tests of the alumina plate and glass, and the fracture energy was calculated as the area enclosed by the stress–strain curve. The Poisson's ratio and CTE of the interface were the average of the values for the glass and Al_2O_3, and the other properties were obtained from the literatures.

Models of 100 μm × 100 μm, 10 μm × 10 μm and 1 μm × 1 μm were established for GC2, GC3 and GC4, respectively, with loads of 1, 0.1 and 0.01 N. Different sizes of GC1 models without reinforcement particles verified that the normalized crack length and crack form would not be affected by the model size and load. Two analysis steps were set. The first analysis step applied a temperature load of 500 °C to room temperature, and the second analysis step applied a concentrated force on the model, as shown in Fig. 2. The Nlgeom function in step 2 was activated to simulate the fracture process. For plane stress analysis of samples, 4-node bilinear quadrilateral elements with reduced integration and hourglass control (CPS4R) were adopted [45]. The number of elements was approximately 50, 000. The crack geometry was completely independent of the mesh in XFEM, and detailed element research or remeshing was not required [46,47]. The crack length and morphology were recorded for subsequent analysis.
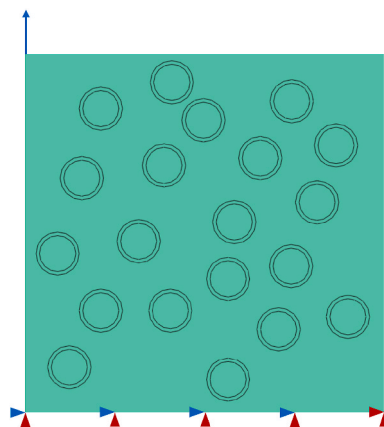

Fig. 2. The boundary conditions and loads of the model.

Table 2
Mechanical and physical properties used in this model.

| Properties	Glass	Reference	Al$_2$O$_3$	Reference	Interface
Young's modulus (GPa)	73	–	214	–	128
Poisson's ratio	0.33	[37]	0.22	[8]	0.28
CTE (10^{-6}/°C)	variable	–	8.4	[8]	7.7
Max principal stress (MPa)	40	[37]	260	[43]	21.3
Fracture energy (J/m^2)	4.42	[37]	20	[44]	3.47

3. Results and discussion

3.1. Parametric study

3.1.1. Interfacial properties of glass matrix composites

The main strengthening mechanisms of the particles are interface debonding and particle breakage. In composites, the interface properties of the matrix and reinforcement particles are the key conditions for ensuring load transfer and improving performance. In a certain range, the higher the interface strength is, the more it can transfer stress and strain to reinforcement particles with better strength, leading to better properties of the composite. During crack propagation, however, interface debonding will absorb energy and unload stress, thereby reducing the stress concentration and average stress in the matrix. Particle breakage can also absorb energy; thus, sometimes particle breakage is a beneficial phenomenon for helping the material withstand more damage. Therefore, to obtain preferable composites, it is necessary to determine the appropriate interface strength by adjusting the sintering temperature. The shear strength between pure glass powder and alumina plate at different sintering temperatures in the range of 880–1000 °C was measured, and then a large number of reinforcement particles (10 μm, 50 wt%) were added to the glass to measure the compressive strength and observe the fracture surface morphology. The results are shown in Figs. 3 and 4. Fig. 3 shows that the shear strength of the interface between glass and alumina increases from 8.7 MPa to 26.2 MPa with increasing sintering temperature, indicating that a higher sintering temperature can promote wetting and thus improve the interface strength. However, the compressive strength of the glass bulk reaches an extreme value of 207.0 MPa at 960 °C. The reason for the mismatch between compressive and shear strength can be found in the microstructure.

Fig. 4(a–d) shows the microstructure of the fracture surface of composites sintered in the temperature range from 880 °C to 1000 °C. The fracture surface of the glass is relatively smooth, while the surface of the particles is rough. There are two forms of particles, the debonding particles have a spherical convex surface, and the broken particles have a significantly different circular from the surrounding glass. Fig. 4(e) and (f) reveal the morphology of interface debonding and particle breakage at a greater magnification. When samples are sintered at 880 °C, almost all the failure modes are interface debonding rather than particle breakage. As the sintering temperature increases, more particle breakage occurs at the fracture surface, and almost all the particles break at 1000 °C. More energy is needed for particle breakage at the beginning, but crack propagation easily occurs due to the brittleness of alumina. In contrast, the initiation of interfacial debonding requires less energy, but the energy is continuously consumed due to continuous crack deflection. To consume more energy, the interface strength should be improved as much as possible, but a large number of particle fractures should be avoided. Therefore, 960 °C was selected as the sintering temperature to achieve the optimal composite properties.

3.1.2. Effect of reinforcements on porosity

In general, reinforcements may lead to changes in the size and number of bubbles in glass. Bubbles can affect the performance of the
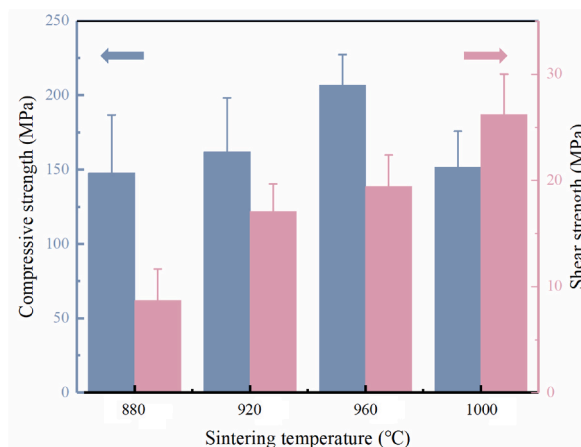
Fig. 3. Compressive strength and shear strength of glass composites sintered at different temperatures.
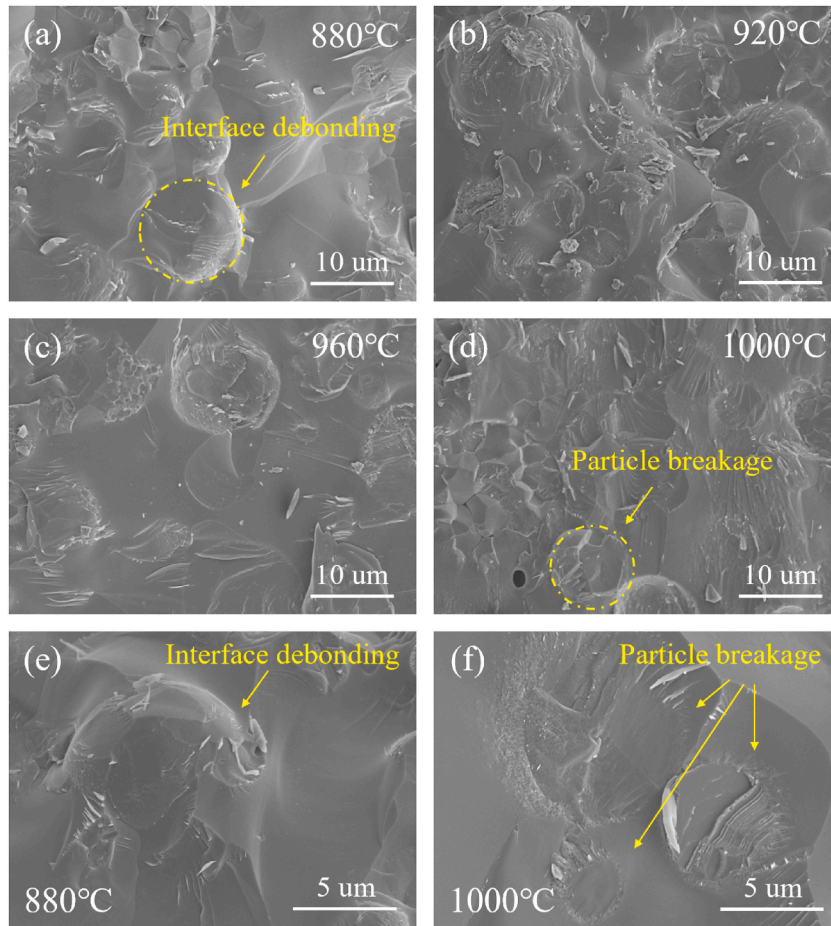
Fig. 4. Morphology of glass composites sintered at different temperatures. (a–d) 880 °C, 920 °C, 960 °C, 1000 °C. (e) Interface debonding morphology. (f) Particle breakage morphology.

composite and must be excluded. The diameters of 200 bubbles in a certain area of the microstructure were measured by ImageJ software, and the bubble distributions of GC1, GC2, GC3 and GC4 were obtained as shown in Fig. 5. The background of Fig. 5 is the SEM image of the samples, in which the size and number of bubbles can be clearly seen. The yellow line indicates the probability of bubbles of different sizes appearing. The porosities of GC1, GC2, GC3 and GC4 are 4.3 vol%, 2.3 vol%, 2.4 vol% and 3.3 vol%, respectively, and the standard deviations of bubble diameter are 5.86, 7.15, 6.07 and 6.63, respectively. The addition of spherical Al_2O_3 decreases the porosity of bubbles but makes the diameter distribution more dispersed. According to previous experimental results [37], the variation in porosity between the four samples has little effect, and the influence of the size of the reinforcements will be highlighted without considering that of porosity.

3.2. Mechanical properties

3.2.1. Static mechanical properties

The hardness of the samples is shown in Table 3. Adding 20 wt% spherical alumina to the glass matrix significantly improves the hardness. When the diameter of the alumina particles is 0.1, 1 and 10 μm, the hardness is increased by 157, 233 and 215, respectively. The enhancement effect of GC2 is significantly weaker than that of GC3 and GC4. The difference between sample GC2 and samples GC3 and GC4 may be mainly due to the interface area. The excessive interface area in GC2 leads to a "softer" material and lower hardness. Therefore, larger reinforcement particles will yield composite materials with higher hardness.

The load−displacement curves of representative GC1, GC2, GC3 and GC4 samples are shown in Fig. 6, and the extreme load values are 7.35, 8.58, 9.00 and 10.2 kN, respectively. The embedding of alumina increases the compressive strength of glass, and the larger the particles are, the more obvious the enhancement effect. In the early stage of loading, GC1 is significantly different from the other samples, with a linear relationship between load and displacement, while the other samples display a downward hump. This indicates that the pure glass is an elastic material at room temperature, and its elastic modulus does not change, while the mechanical properties of the glass matrix composites are more complicated. The slope of the load−displacement curve represents the elasticity of the
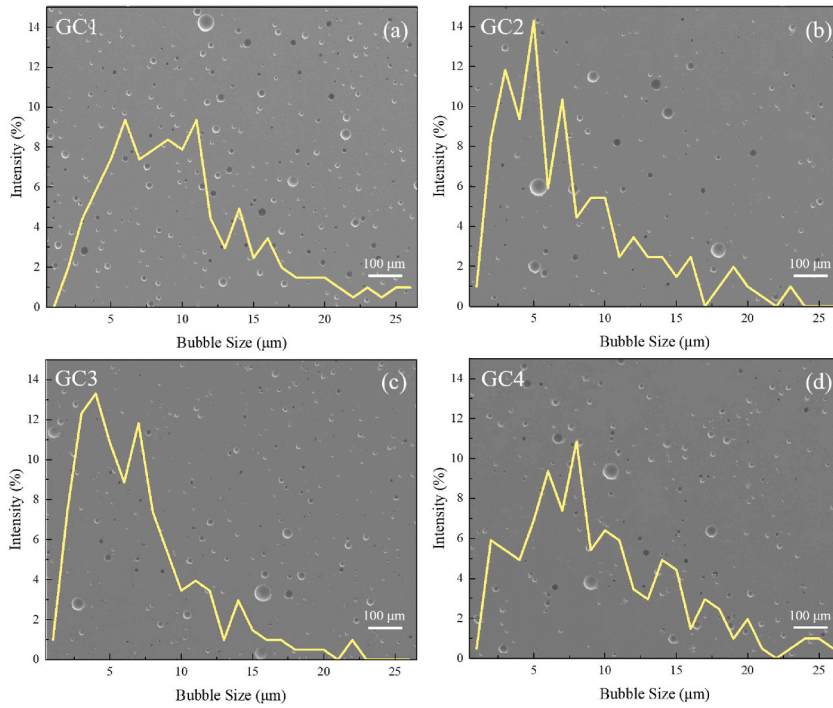
Fig. 5. The bubble distribution and microstructure of (a) GC1, (b) GC2, (c) GC3 and (d) GC4.

Table 3
The hardness, fracture toughness and simulated normalized crack length of the samples, with standard deviations in parentheses.

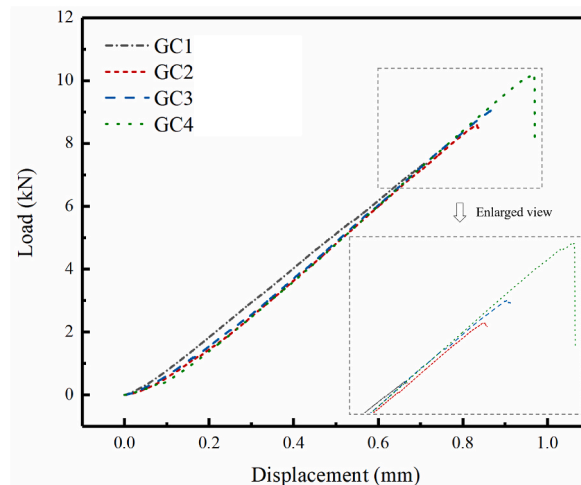|	GC1	GC2	GC3	GC4
Hardness (HV)	473(43)	630(40)	706(37)	688(49)
Fracture toughness (MPa·m$^{0.5}$)	0.48(0.05)	0.82(0.10)	0.76(0.10)	0.73(0.10)
Normalized crack length in simulation	32.5	17.0 (3.8)	18.4(5.8)	22.8 (4.7)

Fig. 6. The load–displacement curves of the samples.

material, and a large slope indicates that the material is not prone to deformation. Therefore, the composite is more ductile than pure glass at the initial stage of loading, but the composite becomes more rigid than pure glass when it is about to fracture according to the curves in the enlarged view. In general, the addition of alumina improves the compressive strength, and the enhancement effect of

large particles is more obvious. On the other hand, alumina makes the composite more ductile in the initial stage of loading, which is the main service stage, so the composite has greater toughness to resist cracks. When the load is large, the compressive strength of the composites is improved due to the larger slope.

3.2.2. Dynamic mechanical properties

The storage modulus and loss modulus of the samples in the range of room temperature to 400 °C were obtained by DMA, and the results are shown in Fig. 7. The storage modulus represents the energy stored in the material due to elastic deformation, reflecting the elastic behavior of the material, that is, the ability to resist deformation. The loss modulus is the ability of the material to consume energy during deformation, reflecting the viscous behavior of the material, and can predict the toughness of the material before crack initiation. The toughness after crack initiation is determined by the fracture toughness, as discussed in Section 3.3.1. As shown in Fig. 7, with increasing temperature, the storage modulus decreases steadily, and the loss modulus increases first and then decreases. The trend of different samples with temperature is very similar. By embedding alumina particles into the glass, the storage modulus and loss modulus are significantly improved. That is, before the initiation of microcracks, the composites with alumina particles can resist more loads and consume more energy. The improvement of GC3 (1 μm) is the most obvious. Consistent with the hardness, GC3 possesses the best performance before crack initiation, which indicates that the appropriate particle size can improve the thermal mechanical properties of composites more efficiently.

3.3. Fracture properties

3.3.1. Fracture toughness and FEA

The crack length was measured by SEM after indentation, and the fracture toughness of the composites was calculated by Eq. (1), with the results shown in Table 3. After embedding 20 wt% spherical alumina with a diameter of 0.1, 1 and 10 μm, the fracture toughness of the glass increases by 1.72, 1.60 and 1.53 times, respectively, which indicates that smaller particles are more effective in improving fracture toughness. The simulation results exhibit a similar trend in which the crack length is reduced to 0.52, 0.57 and 0.70 of the original length, respectively (as shown in Table 3). These phenomena can be explained at the microscale. Fig. 8 shows the fracture surfaces of the samples. In GC1 (Fig. 8(a)), the fracture surface is significantly smoother and flatter than other samples because the crack propagation is not hindered by reinforcement particles. The fracture surface morphologies of GC2, GC3 and GC4 become increasingly rough with increasing particle diameter, and there are obvious differences between them. In Fig. 8(e), with a larger magnification, it can be seen that almost all the particles are peeled off from the matrix due to the small particle diameter and the low energy required for peeling. The fracture toughness values indicate that the accumulated energy consumed by this small-scale peeling will greatly improve the fracture toughness of the composites. However, more particles are broken in GC3 and GC4 (Fig. 8(c, d, f)), and crack deflection makes the fracture surface undulate. Particle breakage and crack deflection are the main reasons for energy consumption in GC3 and GC4, which is effective in improving the fracture toughness of the materials, but the effect of larger particles is slightly worse than that of smaller particles. The more obvious toughening effect of small particles may be due to the large interface area and the greater tendency for interfacial debonding.

The normalized crack lengths from the simulation are listed in Table 3, with a trend similar to that obtained by the indentation method, but the standard deviation is larger, which may be affected by the parameter settings. This proves that smaller reinforcement particles would improve the fracture toughness to a greater degree. The crack morphology from the finite element results is shown in Fig. 9. In pure glass (GC1), the crack propagates perpendicular to the loaded concentrated force, with almost no deflection. The normalized crack lengths in different scales of GC1 are equal, so there is no standard deviation of the value in Table 3. For composites with reinforcement particles, cracks interact with the particles, leading to deflection or traversal. In Fig. 9(d), the crack enters the particle and stops in it. The fracture toughness of alumina particles is larger than that of glass, so the cracks tend to stop in the
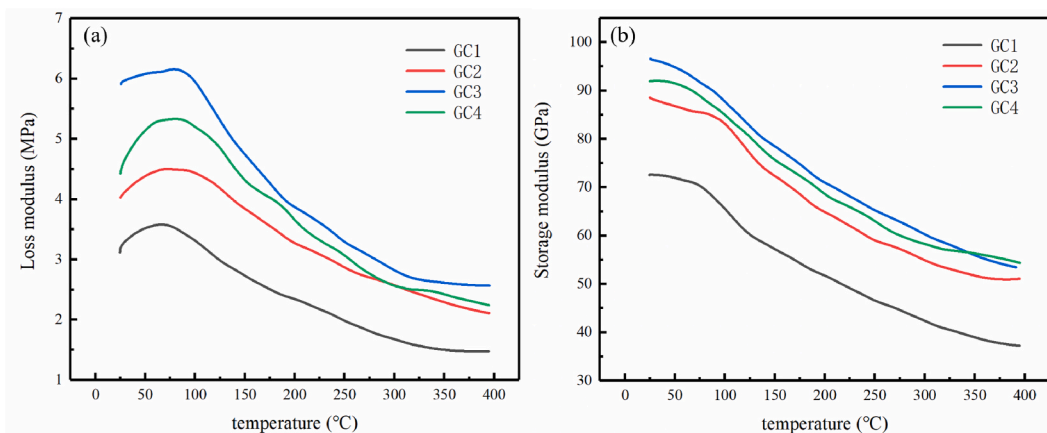

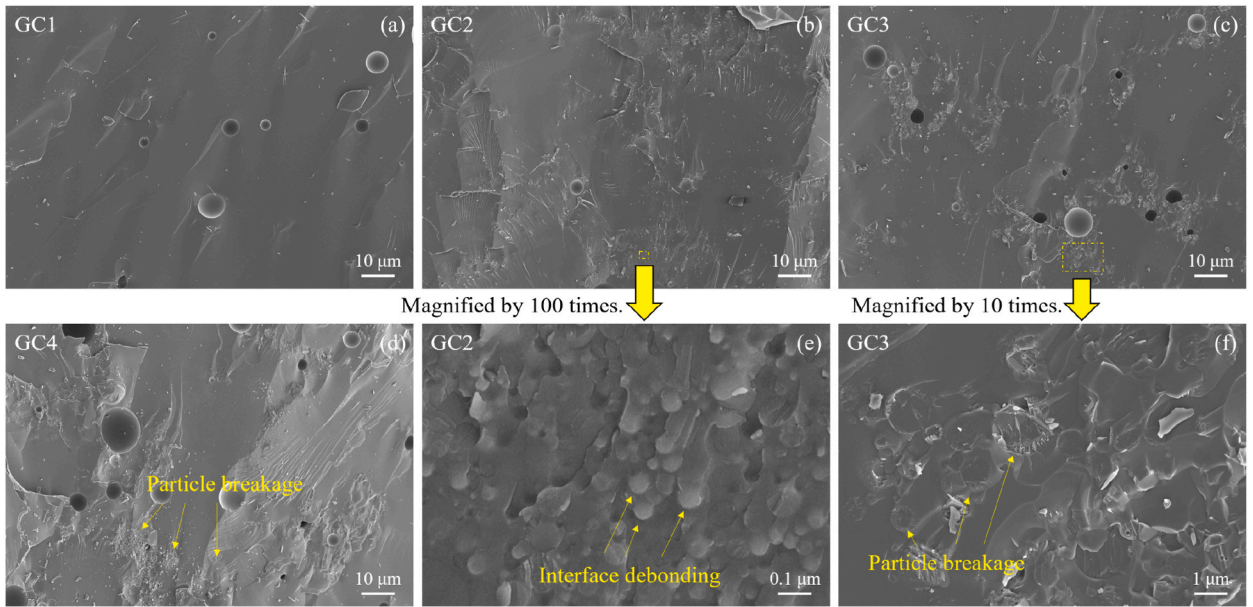**Fig. 7.** (a) Storage modulus and (b) loss modulus of samples.

Fig. 8. Fracture surfaces of (a) GC1, (b, e) GC2, (c, f) GC3, and (d) GC4.
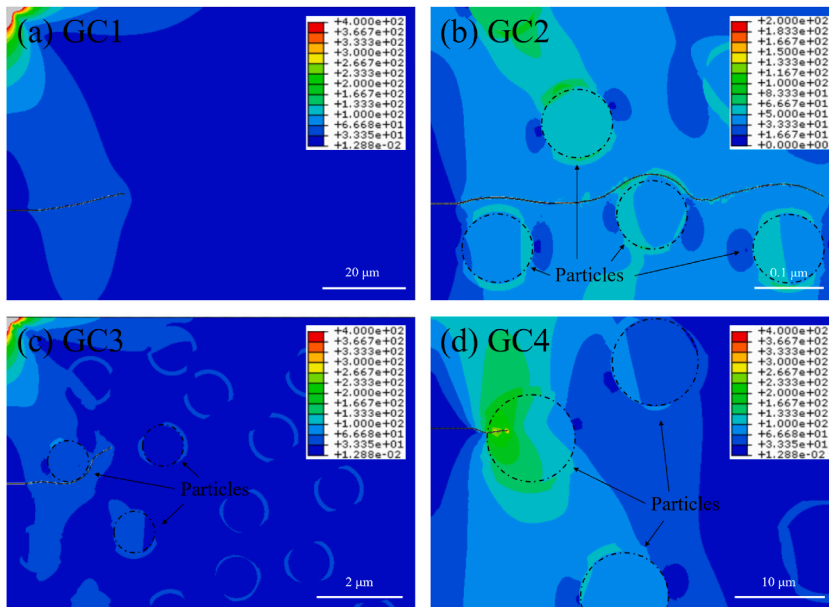

Fig. 9. Simulated cracks in different samples: (a) GC1, (b) GC2, (c) GC3, and (d) GC4.

reinforcement particles, which results in toughening. In Fig. 9(c), the crack propagates along the interface and deflects continuously after extending to the interface, which consumes considerable fracture energy. In Fig. 9(b), even if the crack is not in contact with the reinforcement particles, it will still be attracted and deflected due to the fluctuating stress near the particles, thus forming wavy cracks and consuming the fracture energy. Moreover, the simulation results indicate that the angle between the crack and the particle greatly affects the behavior of the crack. This issue will be explored in the next section.

3.3.2. Hypothesis testing

To explore the relationship between cracks and reinforcement particles, the microscopic morphology of cracks that interact with particles is shown in Fig. 10. Similar to the simulation, the crack of pure glass propagates straight (Fig. 10(a)). Its fracture toughness is the lowest, and the crack length is the longest under the same load. After reinforcement particles are embedded into the glass matrix,
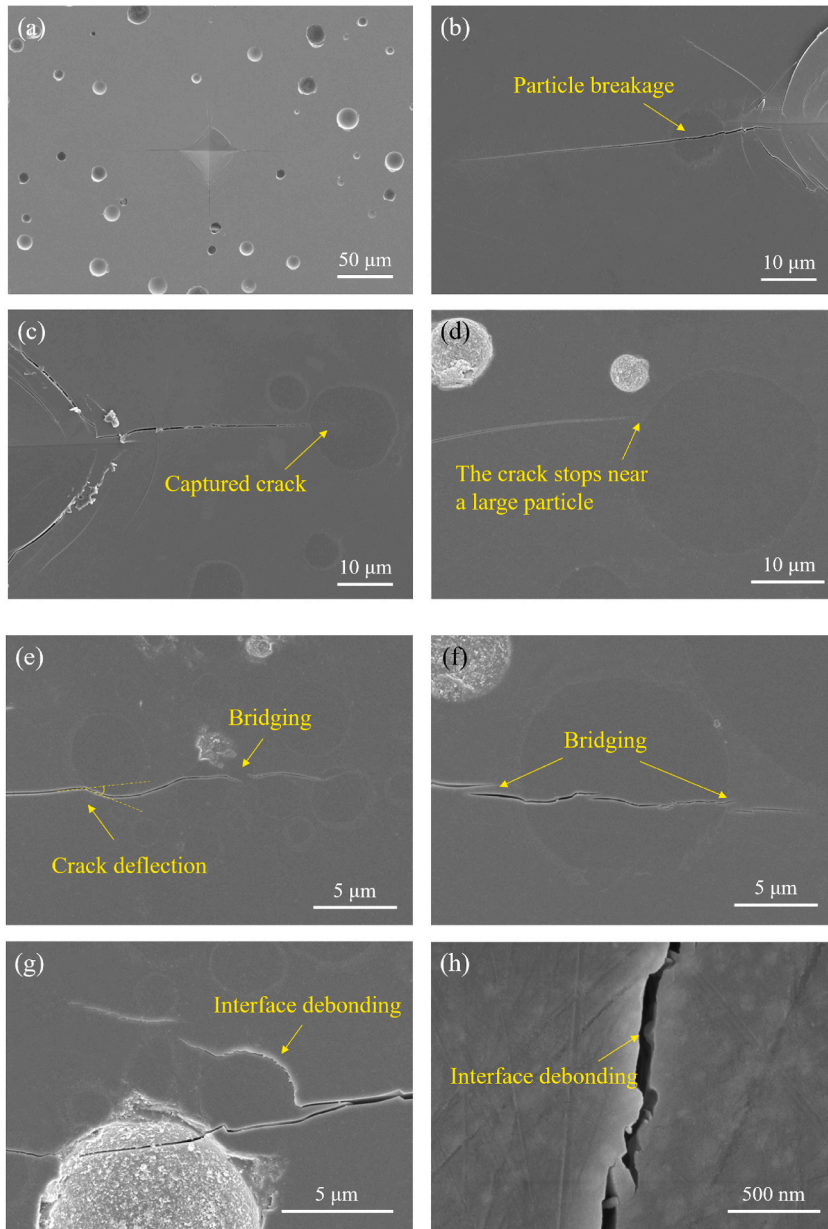
Fig. 10. Crack morphology. (a) The indentation morphology of GC1. (b) The crack traverses the particle. (c) The crack stops inside the particle. (d) The crack stops near the particle. (e) The crack deflects and bypasses the particle, and bridging occurs at the crowded particles. (f) The cracks are bridged near larger particles several times. (g) Crack deflection and interfacial debonding. (h) Interface debonding and bridging in GC2 (100 nm).

interactions between the cracks and ceramic particles will occur. If the contact angle between the crack and the particle is large (nearly 90°, as shown in Fig. 10(b and c)), the particle will split when the fracture energy is large, and a crack with less energy will be captured and stopped in the particle. Cracks with small fracture energy are also likely to stop near large particles because the compressive stress along the crack propagation direction is large adjacent to such particles (Fig. 10(d)). The fluctuation of stress leads to crack bridging, which is prone to occur at areas of particle aggregation (Fig. 10(e)) or near large particles (Fig. 10(f)). Bridging consumes a large amount of fracture energy and improves fracture toughness. Debonding rarely occurs near micron particles (Fig. 10(g)) but frequently occurs when nanoparticles interact with cracks, accompanied by bridging (Fig. 10(h)).

To explore the influence of particle diameter and contact angle between cracks and particles on the propagation direction, 100 cracks interacting with reinforcement particles were observed and recorded by SEM for hypothesis testing [48]. The data were evenly divided into 4 or 5 groups, and an irrelevant hypothesis (H_0) was assumed. The original hypothesis can be expressed as:

$$H_0 : n_{ij} = \frac{n_i . n_{.j}}{n}, i = 1, \ldots, k, k = 4, 5, j = 1, 2 \tag{2}$$

Accordingly, the test statistic is:

$$\chi^2 = \sum_i \sum_j \frac{\left(n_{ij} - \frac{n_i . n_{.j}}{n}\right)^2}{\frac{n_i . n_{.j}}{n}} \tag{3}$$

The pchisq function in R-studio was used to calculate χ^2 and the P value, and the probability that the original hypothesis does not hold was obtained. The corresponding values are shown in Table 4, which shows that the traversal (particle breakage) of micron-sized particles or deflection (interface debonding) during crack propagation mainly depends on the contact angle between the particle and crack (confidence level: 99.9 %, 82.6 %) rather than the diameter of the particle (confidence level: 18.3 %, 55.7 %). In other words, the influence of particle diameter on fracture toughness is caused by the contact angle between the particle and crack. Particles with large curvature are more likely to cause interface debonding and consume more energy. From the perspective of fracture properties, particles with larger curvature have a better improvement effect, while in terms of mechanical properties, particles with a larger diameter have a better enhancement effect. Therefore, the reinforcement particles with larger curvature and larger diameter shown in Fig. 11 will have all the above advantages, that is, the mechanical strength of large particles and the fracture toughness of small particles.

4. Conclusion

In this paper, static and dynamic mechanical tests, fracture toughness tests, microstructure analysis and finite element analysis were employed to explore the effect of reinforcement particle size on the mechanical and fracture properties of glass matrix composites. It is concluded that the size of the reinforcement affects the mechanical properties by changing the contact angle between cracks and particles. The following are the key findings.

- In alumina-reinforced glass matrix composites, the mechanism of reinforcement is mainly interface debonding and particle breakage. The energy required for the fracture initiation of the particles is high, but crack propagation is easy due to the brittleness of alumina. Conversely, the fracture energy required for the initial debonding of the interface is relatively low. Due to the continuous deflection of cracks along the interface, interface debonding consumes more energy than particle breakage.
- Regarding mechanical properties, the hardness, compressive strength, storage modulus and loss modulus will increase significantly due to the addition of alumina particles, and larger particles have a better enhancement effect. Compared with pure glass, composites are softer and more ductile in conventional service and are more rigid under larger loads, resulting in greater strength.
- Regarding fracture properties, smaller reinforcement particles lead to greater fracture toughness. Based on microstructure analysis and hypothesis tests, it is found that the factor affecting whether a crack splits particles or deflects to bypass particles is not the particle diameter, but the curvature of the particles. Therefore, reinforcement particles with a large diameter and small curvature will result in composites with both excellent mechanical and fracture properties.

Funding

CRediT authorship contribution statement

Yangyang Cai: Conceptualization, Methodology, Software, Writing – original draft. **Zheng Liu:** Validation, Writing – review & editing. **Keqian Gong:** Data curation, Investigation, Visualization. **Yong Zhang:** Resources, Supervision, Writing – review & editing.

Declaration of competing interest

The authors declare that they have no known competing financial interests or personal relationships that could have appeared to influence the work reported in this paper.

Table 4
Hypothesis test results.

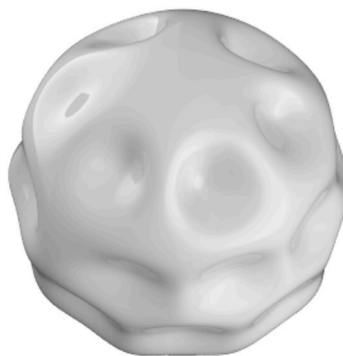|	χ^2	Degree of freedom	P value	Confidence level
Contact angle – traverse	15.5789	3	0.001383	99.8617 %
Contact angle – deflect	4.9636	3	0.174482	82.5518 %
Particle diameter – traverse	1.5548	4	0.816892	18.3108 %
Particle diameter – deflect	3.7334	4	0.443287	55.6713 %

Fig. 11. Ideal shape of reinforcement particles.

Appendix A. Supplementary data

Supplementary data to this article can be found online at https://doi.org/10.1016/j.heliyon.2023.e21895.

References

[1] K. Hu, S. Li, Z. Fan, H. Yan, X. Liang, Y. Cai, et al., Contributions of mechanical bonding and chemical bonding to high-temperature hermeticity of glass-to-metal compression seals, Mater. Des. 202 (2021), 109579, https://doi.org/10.1016/j.matdes.2021.109579.

[2] S. Li, Y. Cai, Q. Zhu, Z. Liu, Y. Zhang, Interface degradation of glass-to-metal seals during thermo-oxidative aging, Corrosion Sci. 199 (2022), 110189, https://doi.org/10.1016/j.corsci.2022.110189.

[3] R. Li, X. Liang, X. Wang, W. Zeng, J. Yang, D. Yan, et al., Improvement of sealing performance for Al$_2$O$_3$ fiber-reinforced compressive seals for intermediate temperature solid oxide fuel cell, Ceram. Int. 45 (2019), 21953, https://doi.org/10.1016/j.ceramint.2019.07.209. –9.

[4] A. Selçuk, A. Atkinson, Measurement of mechanical strength of glass-to-metal joints, Fuel Cells (Weinh) 15 (2015) 595–603, https://doi.org/10.1002/fuce.201500028.

[5] S. Arunkumar, M. Subramani Sundaram, K.M. Suketh kanna, S. Vigneshwara, A review on aluminium matrix composite with various reinforcement particles and their behaviour, Mater Today Proc 33 (2020) 484–490, https://doi.org/10.1016/j.matpr.2020.05.053.

[6] S. Sharma, T. Nanda, O.P. Pandey, Effect of particle size on dry sliding wear behaviour of sillimanite reinforced aluminium matrix composites, Ceram. Int. 44 (2018) 104–114, https://doi.org/10.1016/j.ceramint.2017.09.132.

[7] M.S. Kumar, M. Vasumathi, S.R. Begum, S.M. Luminita, S. Vlase, C.I. Pruncu, Influence of B$_4$C and industrial waste fly ash reinforcement particles on the micro structural characteristics and mechanical behavior of aluminium (Al–Mg–Si-T6) hybrid metal matrix composite, J. Mater. Res. Technol. 15 (2021) 1201–1216, https://doi.org/10.1016/j.jmrt.2021.08.149.

[8] A. Kurşun, E. Bayraktar, H.M. Enginsoy, Experimental and numerical study of alumina reinforced aluminum matrix composites: Processing, microstructural aspects and properties, Compos Part B Eng 90 (2016) 302–314, https://doi.org/10.1016/j.compositesb.2016.01.006.

[9] H. Qing, 2D micromechanical analysis of SiC/Al metal matrix composites under tensile, shear and combined tensile/shear loads, Mater. Des. 51 (2013) 438–447, https://doi.org/10.1016/j.matdes.2013.04.051.

[10] T. Chongcharoenchaikul, K. Miyaji, P. Junkong, S. Poompradub, Y. Ikeda, Synergistic effect of cuttlebone particles and non-rubber components on reinforcing ability of natural rubber and synthetic isoprene rubber composites, J. Appl. Polym. Sci. 139 (2022), 52375, https://doi.org/10.1002/app.52375.

[11] M.R. Parvaiz, S. Mohanty, S.K. Nayak, P.A. Mahanwar, Effect of surface modification of fly ash on the mechanical, thermal, electrical and morphological properties of polyetheretherketone composites, Mater Sci Eng A 528 (2011) 4277–4286, https://doi.org/10.1016/j.msea.2011.01.026.

[12] V. Bocharova, A.-C. Genix, J.-M.Y. Carrillo, R. Kumar, B. Carroll, A. Erwin, et al., Addition of short polymer chains mechanically reinforces glassy poly(2-vinylpyridine)–silica nanoparticle nanocomposites, ACS Appl. Nano Mater. 3 (2020) 3427–3438, https://doi.org/10.1021/acsanm.0c00180.

[13] L. Jong, Particle reinforced composites from acrylamide modified blend of styrene-butadiene and natural rubber, Polym. Compos. 40 (2018) 758–765, https://doi.org/10.1002/pc.24734.

[14] Q. Jiang, C. Cao, T. Lin, S. Wu, X. Li, Strong and tough glass with self-dispersed nanoparticles via solidification, Adv Mater 31 (2019), 1901803, https://doi.org/10.1002/adma.201901803.

[15] A.R. Boccaccini, P.A. Trusty, Toughening and strengthening of glass by Al2O3 platelets, J. Mater. Sci. 15 (1996) 60–63, https://doi.org/10.1007/bf01855614.

[16] A.R. Boccaccini, Sintering of glass matrix composites containing Al$_2$O$_3$ platelet inclusions, J. Mater. Sci. 29 (1994) 4273–4278, https://doi.org/10.1007/bf00414210.

[17] S. Ma, X. Zhang, T. Chen, X. Wang, Microstructure-based numerical simulation of the mechanical properties and fracture of a Ti-Al3Ti core-shell structured particulate reinforced A356 composite, Mater. Des. 191 (2020), 108685, https://doi.org/10.1016/j.matdes.2020.108685.

[18] A. Paknia, A. Pramanik, A.R. Dixit, S. Chattopadhyaya, Content and shape of reinforcements on the behavior of metal matrix composites (MMCs) under tension, J. Mater. Eng. Perform. 25 (2016) 4444–4459, https://doi.org/10.1007/s11665-016-2307-x.

[19] E.A. Diler, R. Ipek, An experimental and statistical study of interaction effects of matrix particle size, reinforcement particle size and volume fraction on the flexural strength of Al–SiCp composites by P/M using central composite design, Mater Sci Eng A 548 (2012) 43–55, https://doi.org/10.1016/j.msea.2012.03.066.

[20] K. Prewo, J. Brennan, High-strength silicon carbide fibre-reinforced glass-matrix composites, J. Mater. Sci. 15 (1980) 463–468, https://doi.org/10.1007/bf00551699.

[21] F.F. Lange, Fracture energy and strength behavior of a sodium borosilicate glass-Al2O3 composite system, J. Am. Ceram. Soc. 54 (1971) 614–620, https://doi.org/10.1111/j.1151-2916.1971.tb16016.x.

[22] L. Liu, F. Ye, Y. Zhou, Z. Zhang, Microstructure compatibility and its effect on the mechanical properties of the α-SiC/β-Si3N4 co-reinforced barium aluminosilicate glass ceramic matrix composites, Scr Mater 63 (2010) 166–169, https://doi.org/10.1016/j.scriptamat.2010.03.040.

[23] R.W. Davidge, The strength of two-phase ceramic/glass materials, J. Mater. Sci. 3 (1968) 629–634, https://doi.org/10.1007/bf00757910.

[24] S. Li, Q. Zhu, K. Hu, Y. Cai, Z. Liu, F. Chen, et al., Determination of compressive stress in glass-to-metal seals using photoluminescence spectroscopy technique, Ceram. Int. 48 (2022) 13379–13385, https://doi.org/10.1016/j.ceramint.2022.01.219.

[25] S.I. Gad, M.A. Attia, M.A. Hassan, A.G. El-Shafei, A random microstructure-based model to study the effect of the shape of reinforcement particles on the damage of elastoplastic particulate metal matrix composites, Ceram. Int. 47 (2021) 3444–3461, https://doi.org/10.1016/j.ceramint.2020.09.189.

[26] M.M.R.A. Lima, R.C.C. Monteiro, M.P.F. Graça, M.G. Ferreira da Silva, Structural, electrical and thermal properties of borosilicate glass–alumina composites, J Alloy Compd 538 (2012) 66–72, https://doi.org/10.1016/j.jallcom.2012.05.024.

[27] J. Watts, G. Hilmas, W.G. Fahrenholtz, Mechanical Characterization of ZrB2-SiC composites with varying SiC particle sizes, J. Am. Ceram. Soc. 94 (2011) 4410–4418, https://doi.org/10.1111/j.1551-2916.2011.04885.x.

[28] O.T. Sanya, B. Oji, S.S. Owoeye, E.J. Egbochie, Influence of particle size and particle loading on mechanical properties of silicon carbide–reinforced epoxy composites, Int. J. Adv. Manuf. Technol. 103 (2019) 4787–4794, https://doi.org/10.1007/s00170-019-04009-1.

[29] F. Chang, D. Gu, D. Dai, P. Yuan, Selective laser melting of in-situ Al4SiC4 + SiC hybrid reinforced Al matrix composites: influence of starting SiC particle size, Surf. Coat. Technol. 272 (2015) 15–24, https://doi.org/10.1016/j.surfcoat.2015.04.029.

[30] Y. Su, Q. Ouyang, W. Zhang, Z. Li, Q. Guo, G. Fan, et al., Composite structure modeling and mechanical behavior of particle reinforced metal matrix composites, Mater Sci Eng A 597 (2014) 359–369, https://doi.org/10.1016/j.msea.2014.01.024.

[31] C.-W. Nan, D.R. Clarke, The influence of particle size and particle fracture on the elastic/plastic deformation of metal matrix composites, Acta Mater. 44 (1996) 3801–3811, https://doi.org/10.1016/1359-6454(96)00008-0.

[32] E.A. Diler, R. Ipek, Main and interaction effects of matrix particle size, reinforcement particle size and volume fraction on wear characteristics of Al–SiCp composites using central composite design, Compos Part B Eng 50 (2013) 371–380,, https://doi.org/10.1016/j.compositesb.2013.02.001.

[33] B. Wang, Y. Qin, F. Jin, J.-F. Yang, K. Ishizaki, Pulse electric current sintering of cubic boron nitride/tungsten carbide–cobalt (cBN/WC–Co) composites: effect of cBN particle size and volume fraction on their microstructure and properties, Mater Sci Eng A 607 (2014) 490–497, https://doi.org/10.1016/j.msea.2014.04.029.

[34] G. Celebi Efe, M. Ipek, S. Zeytin, C. Bindal, An investigation of the effect of SiC particle size on Cu–SiC composites, Compos Part B Eng 43 (2012) 1813–1822, https://doi.org/10.1016/j.compositesb.2012.01.006.

[35] S. Mahdavi, A. Asghari-Alamdari, M. Zolola-Meibodi, Effect of alumina particle size on characteristics, corrosion, and tribological behavior of Co/Al2O3 composite coatings, Ceram. Int. 46 (2020) 5351–5359, https://doi.org/10.1016/j.ceramint.2019.10.289.

[36] S. Li, K. Hu, W. Hui, Y. Cai, Y. Zhang, Shear strength and interfacial characterization of borosilicate glass-to-metal seals, J Alloy Compd 827 (2020), 154275, https://doi.org/10.1016/j.jallcom.2020.154275.

[37] Y. Cai, S. Li, K. Hu, Q. Zhu, Z. Liu, K. Gong, et al., Fracture study of glass with bubbles: multiscale finite element method and experimental facts, Materialia 28 (2023), 101746, https://doi.org/10.1016/j.mtla.2023.101746.

[38] G.R. Anstis, P. Chantikul, B.R. Lawn, D.B. Marshall, A critical evaluation of indentation techniques for measuring fracture toughness: I, direct crack measurements, J. Am. Ceram. Soc. 64 (1981) 533–538, https://doi.org/10.1111/j.1151-2916.1981.tb10320.x.

[39] Q. Zhu, S. Li, K. Hu, X. Liang, Y. Cai, Z. Liu, et al., Enhanced mechanical properties of Al2O3-4J42 joints brazed using Ag–Cu–Ti/Cu/Ag–Cu composite filler, Ceram. Int. 47 (2021) 30247–30255, https://doi.org/10.1016/j.ceramint.2021.07.204.

[40] D. Rahmatabadi, M. Ahmadi, M. Pahlavani, R. Hashemi, DIC-based experimental study of fracture toughness through R-curve tests in a multi-layered Al-Mg (LZ91) composite fabricated by ARB, J Alloy Compd 883 (2021), 160843, https://doi.org/10.1016/j.jallcom.2021.160843.

[41] D. Rahmatabadi, A. Shahmirzaloo, M. Farahani, M. Tayyebi, R. Hashemi, Characterizing the elastic and plastic properties of the multilayered Al/Brass composite produced by ARB using DIC, Mater Sci Eng A 753 (2019) 70–78, https://doi.org/10.1016/j.msea.2019.03.002.

[42] L. Zhao, J. Zhi, J. Zhang, Z. Liu, N. Hu, XFEM simulation of delamination in composite laminates, Compos Part Appl Sci Manuf 80 (2016) 61–71, https://doi.org/10.1016/j.compositesa.2015.10.007.

[43] V.E. Saouma, S.-Y. Chang, O. Sbaizero, Numerical simulation of thermal residual stress in Mo- and FeAl-toughened Al2O3, Compos Part B Eng 37 (2006) 550–555, https://doi.org/10.1016/j.compositesb.2006.02.016.

[44] J. Khajornboon, K. Washijima, T. Shiono, Fracture energy and fracture toughness of in situ calcium hexaluminate (CA6)-Alumina monolithic refractory, KEM 766 (2018) 77–82. https://doi.org/10.4028/www.scientific.net/kem.766.77.

[45] Z. Li, Y. Peng, The base force element method based on the arc-length method for stability analysis, Int J Non Linear Mech 144 (2022), 104088, https://doi.org/10.1016/j.ijnonlinmec.2022.104088.

[46] X. Wang, C. Liu, H. Wang, H. Liu, H. Wu, Comparison of consecutive and alternate hydraulic fracturing in horizontal wells using XFEM-based cohesive zone method, J. Pet. Sci. Eng. 143 (2016) 14–25, https://doi.org/10.1016/j.petrol.2016.02.014.

[47] K. Rodacki, K. Furtak, Numerical analysis of crack development of timber-glass composite I-beams in the extended finite element method (XFEM), Compos. Struct. 209 (2019) 349–361, https://doi.org/10.1016/j.compstruct.2018.01.111.

[48] D. Anderson, D. Sweeney, T.A. Williams, Essentials of Statistics for Business and Economics, South-Western Cengage Learning, Mason, Ohio, 1984.